Title

Measurement of the 160Gd(p,n)160Tb excitation function from 4–18 MeV using stacked-target activation

Authors

Chapman, Ryan K
Voyles, Andrew S
Gharibyan, Narek
et al.

Publication Date

2021-05-01

DOI

10.1016/j.apradiso.2021.109647

Peer reviewed

Applied Radiation and Isotopes 171 (2021) 109647

Contents lists available at ScienceDirect

Applied Radiation and Isotopes

journal homepage: www.elsevier.com/locate/apradiso

Measurement of the ^{160}Gd(p,n)^{160}Tb excitation function from 4–18 MeV using stacked-target activation

Ryan K. Chapman [a], Andrew S. Voyles [b], Narek Gharibyan [c], Lee A. Bernstein [b,d], James E. Bevins [a,*]

[a] Department of Engineering Physics, Air Force Institute of Technology, WPAFB, OH 45433, USA
[b] University of California, Berkeley, Berkeley, CA 94720, USA
[c] Lawrence Livermore National Laboratory, Livermore, CA 94551, USA
[d] Lawrence Berkeley National Laboratory, Berkeley, CA 94720, USA

ARTICLE INFO

Keywords:
Gd + p
Gadolinium
^{160}Tb
Nuclear cross section
Stacked-target activation
MCNP
Radioisotope production

ABSTRACT

The ^{160}Gd(p,n)^{160}Tb excitation function was measured between 4–18 MeV using stacked-target activation at Lawrence Berkeley National Laboratory's 88-Inch Cyclotron. Nine copper and eight titanium foils served as proton fluence monitor foils, using the ^{nat}Cu(p,x)^{65}Zn, ^{nat}Ti(p,x)^{48}V, and ^{nat}Ti(p,x)^{46}Sc monitor standards, respectively. Variance minimization using an MCNP v.6.2 model reduced the systematic uncertainties in proton energy and fluence. *A priori* predictions of the ^{160}Gd(p,n) reaction using ALICE, CoH, EMPIRE, and TALYS, as well as the TENDL database, are compared to the experimentally measured values.

1. Introduction

Nuclear data are fundamental for radiation transport, and incorrect or poorly-characterized nuclear data can drastically affect the results obtained. This is the case for charged-particle reactions where evaluations and experimental data are limited and/or not well-characterized, thereby limiting their usefulness as an input into radiation transport simulations. For nuclear forensics, which examines nuclear and non-nuclear materials using analytical techniques to identify their origin in the context of nuclear security and proliferation, simulations often represent a necessary method to determine isotopic inventories. However, since modeling of charged-particle excitation functions often lack even modest (within 20%) predictive capabilities (Voyles et al., 2018, 2019), the absence of measured cross section data can greatly impact the simulated production rates and result in non-realistic distribution of fission and activation products in post-detonation debris (Anon, 2010, 2015; Joint Nuclear Forensics Working Group of the American Physical Society and the American Association for the Advancement of Science, 2013).

More specifically for post-detonation nuclear forensics, the ratio of ^{161}Tb: ^{160}Tb allows for background correction of ^{161}Tb, an important fission product for fission split determination (Nethaway, 1985). As such, ^{160}Tb is routinely included in surrogate debris samples utilized in exercising post-detonation laboratory analysis capabilities. Improvements in the ^{160}Gd(p, n) ^{160}Tb excitation function provides the necessary nuclear data for optimizing the production of post-detonation surrogate debris samples.

Currently, only two experimental measurements of ^{160}Gd(p, n) ^{160}Tb have been performed to date. Vermeulen et al. (2012) took data in the 13–65 MeV energy range using a stacked foil technique and compared a series of ^{nat}Gd(p, x) reaction cross sections to existing nuclear models. Birattari et al. (1973) performed measurements ranging from 4–50 MeV, with the purpose of comparing ^{160}Gd(p, x) reactions to those predicted by a nuclear model in development. Vermeulen and Birattari have two and seven experimental data points, respectively, that overlap with the energy range in this work. These measurements differ from each other and the TENDL-2019 evaluation by tens of percent up to a ~80% at higher energies, as shown in Fig. 1 (Vermeulen et al., 2012; Birattari et al., 1973; Koning et al., 2019).

Using methods similar to those established by Graves, Voyles, and Morrell, this measured the ^{160}Gd(p, n) ^{160}Tb excitation function utilizing a stacked-target activation technique and natural gadolinium foils (Voyles et al., 2018; Graves et al., 2016; Morrell et al., 2020). Iterative simulations of proton transport are used to reduce systematic uncertainties in key quantities such as proton energy and fluence. The measurements made over the 4–18 MeV energy range are then compared to previous measurements and available nuclear data evaluations

* Corresponding author.
E-mail address: James.Bevins@afit.edu (J.E. Bevins).

https://doi.org/10.1016/j.apradiso.2021.109647
Received 17 November 2020; Received in revised form 7 February 2021; Accepted 11 February 2021
Available online 16 February 2021

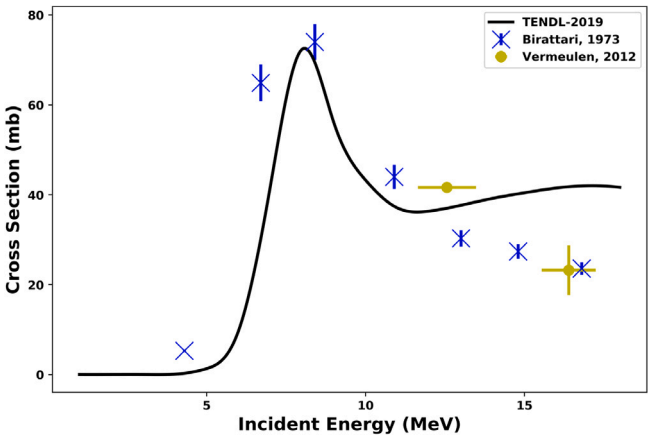

Fig. 1. Comparison of existing experimental data to TENDL-2019 (Vermeulen et al., 2012; Birattari et al., 1973).

and *a priori* predictions using ALICE, CoH, EMPIRE, and TALYS (Blann and Bisplinghoff, 1982; Kawano et al., 2010; Herman et al., 2007; Koning and Rochman, 2012).

2. Materials and irradiation overview

2.1. Facility overview

The proton irradiation took place at Lawrence Berkeley National Laboratory's 88-Inch Cyclotron (Covo et al., 2018). The 88-Inch Cyclotron is a variable-beam, variable-energy K=140 isochronous cyclotron. It has a maximum proton energy of 60 MeV and a maximum proton beam current of ~20 μA. The beam can be extracted for use in experiments in seven separate "caves", which are shown in Fig. 2. Cave 02 was utilized for this experiment.

2.2. Stacked-target design

A target stack was designed to measure the ^{160}Gd(p, n) ^{160}Tb reaction cross section in fifteen separate natural abundance gadolinium foils (Voyles et al., 2018; Graves et al., 2016; Morrell et al., 2020). The stacked-target design maximized the number of proton fluence monitors (copper and titanium) while maintaining approximately even energy spacing for the gadolinium measurements across the 4–18 MeV energy range. An MCNP v6.2 (Anon., 2017) model was developed of the stacked target using runs of 10 million protons to model charged-particle energy loss throughout each layer of the foil stack.

The 18.0 MeV proton beam was modeled as a mono-directional beam along the x-axis, centered in the y–z plane for the foil stack. The beam was modeled with a Gaussian energy spread of 2% (Voyles et al., 2019; Morrell et al., 2020). Each foil in the stacked target was modeled using the measured geometry of each foil (length width, thickness, and density) in the MCNP input deck. The dimension and propagated measurement uncertainties for each foil used in the final stack are shown in Table 1. The areal densities used were calculated from the measured mass and foil areal dimensions. The MCNP models used the default ENDF/B-VII.1 libraries for reaction data (Anon., 2017), with the exception of the ^{nat}Gd(p, x) and the ^{nat}Ti(p, x) reactions, which used the evaluations from TENDL-2019's as the ENDF/B-VII.1 ace files were not available (Koning et al., 2019).

Fig. 3 illustrates each of the materials used and their location in the foil stack. The iron foil used at the beginning of the stack was placed on a sheet of self-developing GafChromic film to provide a radiograph of the beam spread to confirm after irradiation. This radiograph showed

Table 1
Measured foil specifications for each foil in the stacked-target. The foils are listed in order of interaction with the incident beam.

Foil	Thickness (μm)	Areal density (mg/cm^2)
Fe	29.0 ± 0.5	19.80 ± 0.09
Cu-01	26.9 ± 0.1	22.29 ± 0.11
Gd-01	11.8 ± 0.2	8.53 ± 0.05
Ti-01	26.2 ± 0.3	11.29 ± 0.06
Cu-02	26.7 ± 0.1	22.24 ± 0.11
Gd-02	9.0 ± 0.1	6.50 ± 0.04
Ti-02	26.7 ± 0.3	11.04 ± 0.06
Cu-03	26.9 ± 0.1	22.21 ± 0.11
Gd-03	11.5 ± 0.1	8.06 ± 0.05
Ti-03	26.4 ± 0.5	11.11 ± 0.06
Gd-04	9.0 ± 0.3	6.40 ± 0.04
Cu-04	26.6 ± 0.1	22.10 ± 0.11
Gd-05	12.7 ± 0.2	9.07 ± 0.05
Ti-04	26.1 ± 0.1	11.04 ± 0.06
Gd-06	12.4 ± 0.2	8.51 ± 0.05
Cu-05	10.6 ± 0.2	8.68 ± 0.05
Gd-07	13.0 ± 0.2	9.31 ± 0.05
Ti-05	25.8 ± 0.4	11.16 ± 0.06
Gd-08	12.7 ± 0.3	9.46 ± 0.05
Cu-06	9.9 ± 0.4	8.38 ± 0.05
Gd-09	11.0 ± 0.2	8.42 ± 0.05
Ti-06	22.6 ± 0.1	11.08 ± 0.06
Gd-10	12.5 ± 0.2	9.23 ± 0.05
Cu-07	9.7 ± 0.1	8.38 ± 0.05
Gd-11	11.6 ± 0.2	8.60 ± 0.05
Ti-07	22.6 ± 0.1	10.99 ± 0.06
Gd-12	11.5 ± 0.1	8.82 ± 0.05
Cu-08	10.1 ± 0.2	8.53 ± 0.05
Gd-13	9.5 ± 0.4	7.02 ± 0.04
Ti-08	25.6 ± 0.2	10.95 ± 0.05
Gd-14	8.8 ± 0.2	6.59 ± 0.04
Cu-09	10.6 ± 0.2	8.77 ± 0.05
Gd-15	10.2 ± 0.3	7.51 ± 0.05
SS	129.6 ± 0.3	104.1 ± 7.3

that the beam was centered and collimated within the first copper foil, Cu-01. The stainless steel foil at the end of the stack functioned as a beam stop and a radiograph taken using it confirmed that the beam remained collimated throughout the stack.

The experimental apparatus, including the sample holder, a titanium monitor foil, a Kapton-encapsulated gadolinium foil, and the stacked-target assembly, are shown in Fig. 4. The 3M® 5413-Series Kapton polyimide film tape was applied to both sides of each gadolinium foil — each piece of tape consists of 43.2 μm of a silicone adhesive (nominal 4.79 mg/cm^2) on 25.4 μm of a polyimide backing (nominal 3.61 mg/cm^2). A small gap between each foil, roughly $\frac{1}{16}$ of an inch, existed due to the thickness of the sample holders, seen in Fig. 4(a). This was neglected in the modeling as the stacked-target assembly is under a 5×10^{-6} torr vacuum.

2.3. Measurement of induced activities

A multi-nuclide source containing ^{241}Am, ^{88}Y, ^{109}Cd, ^{57}Co, ^{123m}Te, ^{51}Cr, ^{113}Sn, ^{85}Sr, ^{137}Cs, and ^{60}Co was used to calibrate an Ortec GEM-F8250P4 (S/N: 51-TP42244 A) High-Purity Germanium (HPGE) detector with a 13-bit digitizer used for the measurement of the induced activities in each foil in this work. The initial counting began approximately 16 days after the end of beam. The efficiency at each of the gamma energies from the multi-nuclide calibration source was fit using an HPGe efficiency function given by:

$$\epsilon = A\ \ln(E_\gamma) + B\frac{\ln(E_\gamma)}{E_\gamma} + C\frac{\ln(E_\gamma)^2}{E_\gamma} + D\frac{\ln(E_\gamma)^4}{E_\gamma} + E\frac{\ln(E_\gamma)^5}{E_\gamma}, \quad (1)$$

where A, B, C, D, and E are fit parameters and E_γ is the gamma decay energy (Kis et al., 1998). An example energy calibration for the 10 cm counting position is shown in Fig. 5.

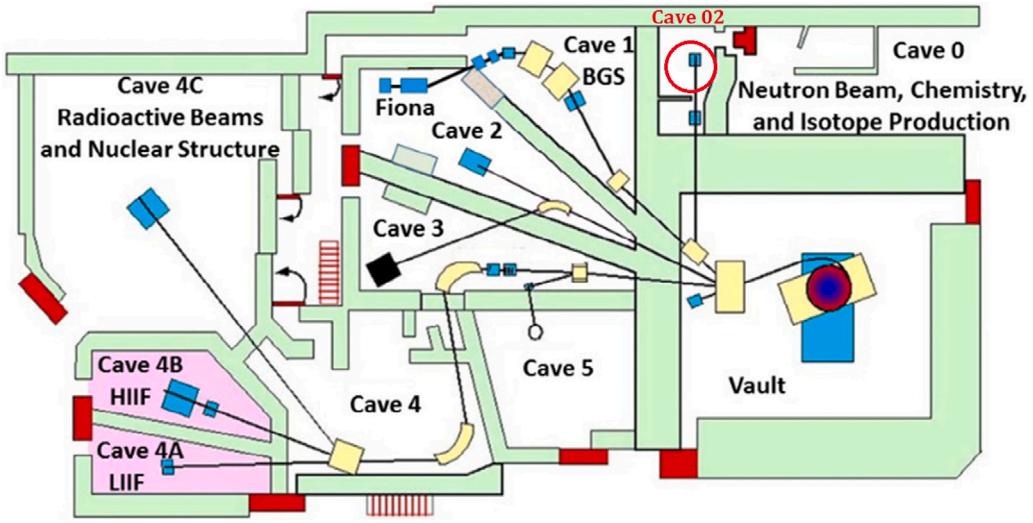

Fig. 2. Schematic of LBNL's 88-Inch Cyclotron displaying each of the beam lines and experimental caves. This experiment was conducted in Cave 02, highlighted in the schematic (Covo et al., 2018).

Fig. 3. Schematic of the stacked target implemented in this work for the order shown in Table 1. All Gd foils were encapsulated in Kapton tape, which is not shown in the schematic.

While Eq. (1) is useful for determining the mean efficiency at a given gamma-ray energy, it does not directly provide any uncertainty quantification. The covariance matrix determined from the curve fit of Eq. (1) using the measured multi-nuclide source activity data was sampled using a multivariate sampling function to generate 10,000 samples of the fit parameters consistent with the covariance in Eq. (1) fit parameters. Gaussian fits were performed for the energy-dependent efficiency probability distributions allowing the extraction of σ to quantify the uncertainty at a given gamma-ray decay energy. The relevant efficiencies and corresponding uncertainties are shown in Table 2.

Using the efficiency from Eq. (1), the end of beam (EOB) activity can be calculated as:

$$A_0 = \frac{C\ \lambda}{(1-e^{-\lambda t_c})e^{-\lambda t_j}\ \epsilon\ f_t\ I_\gamma}, \tag{2}$$

where C is the number of counts in a given peak, λ is the decay constant of the product [s^{-1}], t_j is the amount of time between the end of irradiation and the beginning of a spectrum acquisition [s], t_c is the amount of counting time [s], ϵ is the detector efficiency at the energy corresponding to C from Table 2, f_t is the fraction of live time, and I_γ is the intensity of the gamma decay being measured. Self attenuation was less than 0.1% for all lines measured and was neglected. PeakEasy 4.98.1 was used to determine the counts in each peak from the HPGe gamma spectra (Rooney and Felsher, 2018). The decay constant λ and branching ratios I_γ are obtained from Wu (2000), Burrows (2006), Brown and Tuli (2010) and Reich (2005). For reaction channels with multiple gamma-decay lines, as shown in Table 2, final activities were determined from a correlated uncertainty-weighted mean of the activity from each prominent gamma-decay line (Kauermann and Carroll, 2001).

Due to the thin, ~10–25 μm foils used, the recoiling nucleus can escape and deposit into the next foil. This was seen in the data, primarily with recoils from the titanium and 10 μm copper foils (i.e. thin and "low" Z resulting in longer recoil ranges). No gadolinium recoils were observed in other foils, primarily due to the Kapton encasing. The induced activity for primary gamma-ray decays observed in the immediately subsequent foil was added to the activity observed in the preceding foil to determine the total induced activity. For example, recoils from Cu-05, a 10 μm foil, were observed in Gd-07, the subsequent foil in the foil stack as shown on Table 1. This effect was relatively minor resulting in ~1% increase in induced activity for each foil in which this was observed.

The uncertainty in A_0 is given as:

$$\delta A_0 = A_0\sqrt{(\frac{\delta\epsilon}{\epsilon})^2+(\frac{\delta\lambda}{\lambda})^2+(\frac{\delta C}{C})^2+(\frac{\delta I_\gamma}{I_\gamma})^2+(t_j\Delta\lambda)^2+(t_c\Delta\lambda)^2}. \tag{3}$$

The uncertainty in the fraction of live time is neglected as insignificant. The uncertainty in the efficiency $\delta\epsilon$ is given in Table 2. The uncertainty in counts δC was determined from the uncertainty in the PeakEasy fitting (Rooney and Felsher, 2018). The decay constant uncertainty $\delta\lambda$ and branching ratio uncertainty δI_γ are obtained from Wu (2000), Burrows (2006), Brown and Tuli (2010) and Reich (2005). The uncertainty in the time between the end of irradiation and the beginning of counting δt_j is known to the second for the end of irradiation and beginning of counting. The uncertainty in the counting time δt_j is 0.5 s.

2.4. Proton beam energy

To determine the assigned proton energy for the cross-section measurements, the proton energy distribution was tallied in the MCNP model for each of the Gd foils. Results from this tally are shown in Fig. 6. While the distributions approximately follow a Gaussian distribution, there is a low-energy tail resulting in a slight shift of the mean. This tail is highlighted against a Gaussian fit for the Gd-10 proton energy distribution in Fig. 7.

Therefore, the mean energy is reported as a flux-weighted average $\langle E\rangle$:

$$\langle E\rangle = \frac{\int E\frac{d\phi}{dE}dE}{\int \frac{d\phi}{dE}dE}, \tag{4}$$

where E represents the energy for each proton and $\frac{d\phi}{dE}$ is the differential proton flux obtained from MCNP modeling of proton transport for a

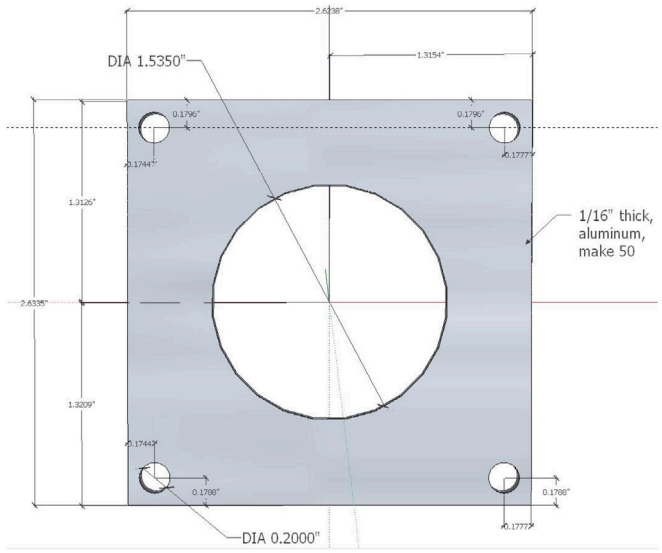

(a) Lucite Slide Schematic

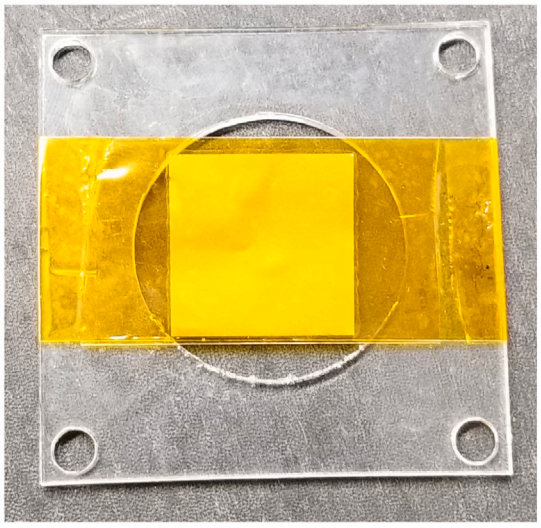

(b) Kapton-Encapsulated Gd Foil

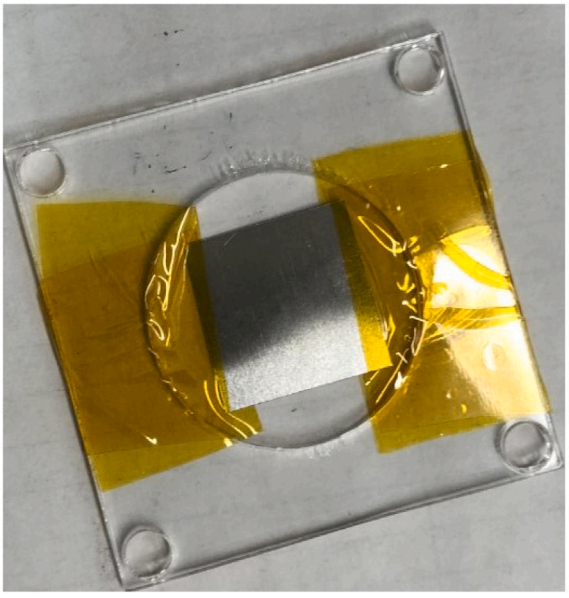

(c) Ti Monitor Foil

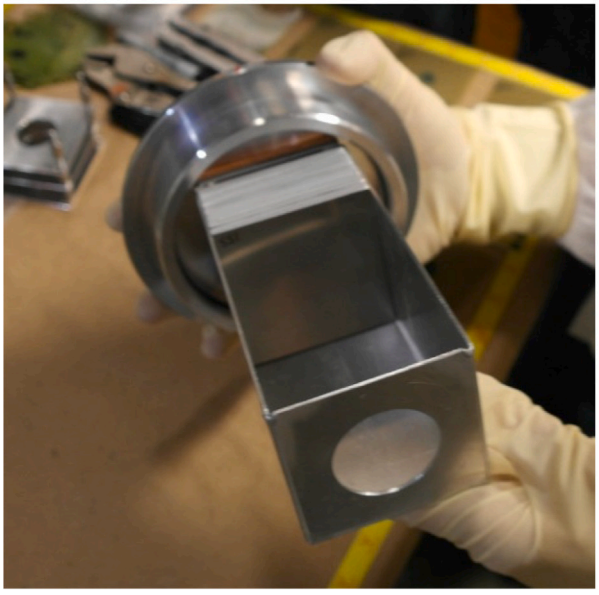

(d) Foil Holding Apparatus

Fig. 4. Schematic of the Lucite sample mount (a) and photos of the mounting strategy for gadolinium (b), titanium and copper monitor foils (c), and the stacked-target assembly (d). The proton beam enters at the window in the bottom of the stacked-target assembly in (d).

Table 2
Relevant gamma-ray decay energies, their intensities and half-lives, and the calibrated efficiencies and relative uncertainty determined using multivariate sampling of Eq. (1) covariance matrix.

Rx product	Gamma-ray energy (keV)	I_γ (%)	$t_{1/2}$	Efficiency	Rel. efficiency uncertainty (%)
^{46}Sc (Wu, 2000)	889.277	99.9840% *10*	83.79 d *4*	0.00191[1]	0.67
	1120.545	99.9870% *10*		0.00161[1]	0.70
^{48}V (Burrows, 2006)	983.525	99.98% *4*	15.9735 d *25*	0.00177[1]	0.69
	1312.106	98.2% *3*		0.00141[1]	0.86
^{65}Zn (Brown and Tuli, 2010)	1115.539	50.004% *10*	243.93 d *9*	0.00160[2]	0.71
^{160}Tb (Reich, 2005)	298.5783	26.1% *6*	72.3 d *2*	0.01049[2]	0.87
	879.378	30.1% *6*		0.00489[2]	0.67
	966.166	25.1% *5*		0.00454[2]	0.69
	1177.954	14.9% *3*		0.00390[2]	0.71

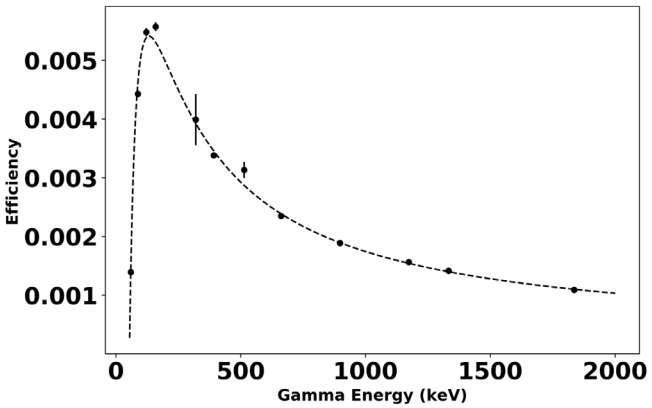

Fig. 5. Example efficiency calibration for the HPGe at the 10 cm counting position, obtained from the multi-nuclide source. Error bars not depicted are smaller than the marker.

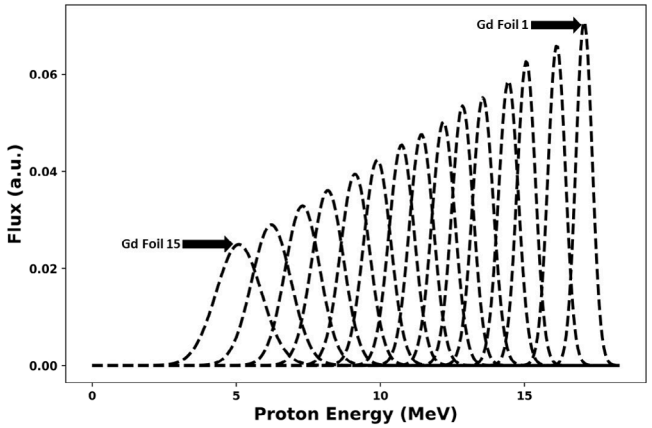

Fig. 6. MCNP-modeled proton energy distributions in each Gd foil.

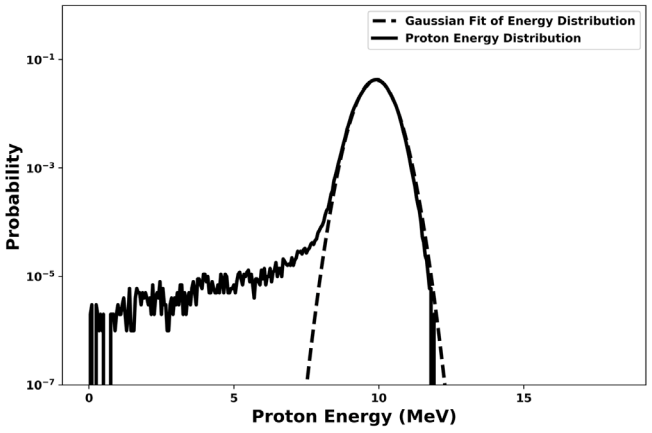

Fig. 7. Proton energy distribution determined from the MCNP model for Gd-10 compared to a Gaussian fit of the data. While the means are similar, there is a shift in the means towards lower energy due to the low-energy tailing seen in the MCNP-modeled proton energy distribution that is not captured in the Gaussian fit.

specific foil (Voyles et al., 2018). Fig. 7 shows the difference between the MCNP-modeled energy distribution and the Gaussian fit for foil Gd-10. The Gaussian fit predicts a mean energy of 9.89 MeV, while the flux-weighted average, used in this work to assign the mean proton energy for each cross section, predicts a mean of 9.87 MeV. The standard deviation determined from the Gaussian fit of each Gd foil

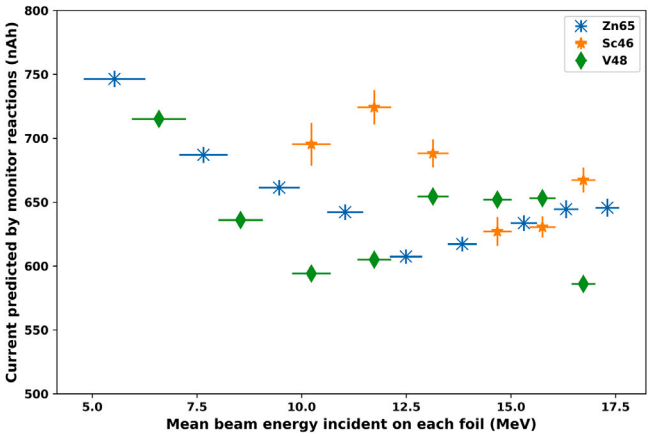

Fig. 8. Monitor foil predicted current as a function of beam energy before variance minimization.

was assigned as the uncertainty in energy space (Voyles et al., 2018, 2019; Graves et al., 2016; Morrell et al., 2020).

2.5. Proton beam fluence

Interlaced throughout the foil stack are several titanium and copper foils, which act both as beam degraders and monitor foils used to determine the proton beam current (Graves et al., 2016). For this work, the ^{nat}Ti(p, x) ^{48}V, ^{nat}Ti(p, x) ^{46}Sc, and ^{nat}Cu(p, x) ^{65}Zn reactions were used. All are well studied and commonly used in stacked foil experiments (Voyles et al., 2018, 2019; Graves et al., 2016; Morrell et al., 2020; Hermanne et al., 2018). The shorter-lived isotopes of each monitor foil were not used due to the delay between irradiation and counting. Consequently, the short-time variations in the beam intensity can be neglected due to the product half-lives being much longer than the time period over which these variations occur. This simplifies the analysis, and only the total proton beam fluence was quantified.

Using these monitor foil reactions, proton beam fluence, in units of nanoampere hours (nAh), can be determined by the relation:

$$I\Delta t = \frac{A_0 \Delta t}{\rho \Delta r (1 - e^{-\lambda \Delta t}) \int \sigma(E) \frac{d\phi}{dE} dE}, \tag{5}$$

where A_0 is the experimentally-measured EOB activity of the monitor foils [Bq] from Eq. (2), Δt is the irradiation time [s], $\rho \Delta r$ is the areal number density of the monitor foil $[\frac{\#}{cm^2}]$, λ is the decay constant in [s^{-1}] of the monitor foil reaction product (Wu, 2000; Burrows, 2006; Brown and Tuli, 2010), $\sigma(E)$ is the IAEA recommended cross section [cm^2] at energy E (Hermanne et al., 2018), and $\frac{d\phi}{dE}$ is the differential proton fluence determined using MCNP and illustrated in Fig. 7 (Voyles et al., 2018). The resulting proton fluences for the monitor reaction data are shown in Fig. 8.

As can be seen, this data is scattered and not physically realistic, as the apparent proton current increases towards the rear of the stack (i.e. at low beam energies). This is primarily due to the systematic uncertainty in three quantities that were not measured directly, resulting in an inaccurate evaluation of $\int \sigma(E) \frac{d\phi}{dE} dE$ in Eq. (5): the incident beam energy, proton stopping power, and Kapton foil areal density.

2.6. Variance minimization

The MCNP model was used to vary the Kapton density and the initial beam energy using MCNP's pStudy (Brown et al., 2004). Beam energy was varied between 17.8–18.2 MeV (±1.1% of the nominal 18.0 MeV) based upon variances seen in past experiments at LBNL's 88-Inch cyclotron (Voyles et al., 2019; Morrell et al., 2020). The areal

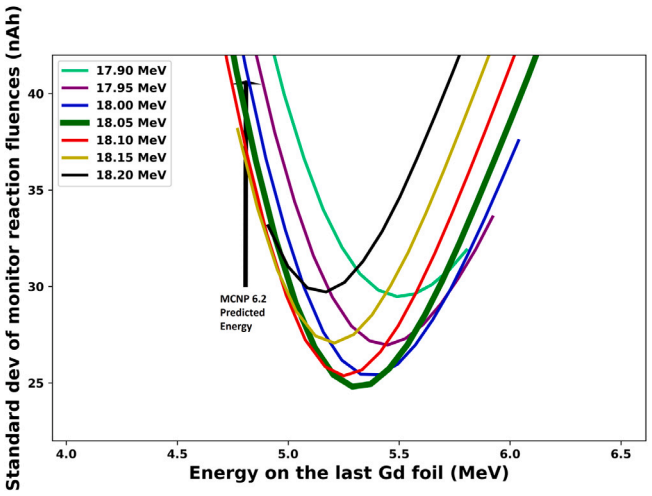

Fig. 9. Results from variance minimization as a function of average proton energy in Gd-15. Each curve represents a variation of the Kapton areal density for a given incident beam energy. The minimum standard deviation of the monitor data was an incident beam energy of 18.05 MeV and a Kapton areal density that was 96% of nominal. This resulted in a flux-weighted average energy of 5.3 MeV in Gd-15, compared to 4.8 MeV using the nominal Kapton areal density and beam energy of 18.0 MeV.

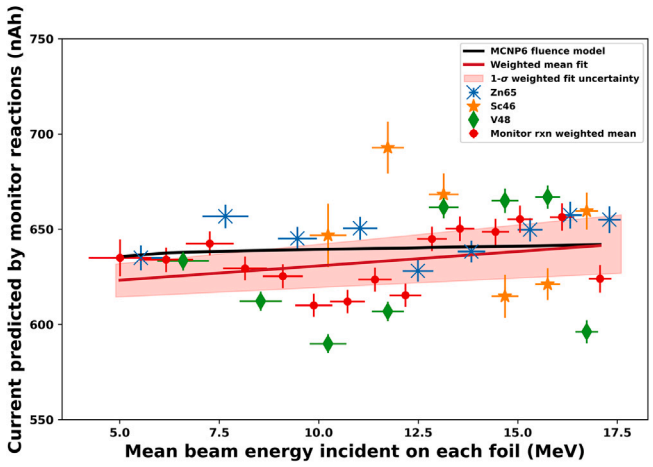

Fig. 10. Final mean proton fluences throughout the target stack, based on the variance-minimized observed fluence from the ^{nat}Cu(p, x) ^{65}Zn, ^{nat}Ti(p, x) ^{46}Sc, and ^{nat}Ti(p, x) ^{48}V monitor reactions. MCNP6 uncertainties, not shown, were $\ll 0.1\%$ at all points. The fluence drops by approximately 2.8% from the incident fluence of 641.4 ± 15 nAh.

density of the Kapton tape (including adhesive) were varied between 0.95–1.05% of the nominal manufacture stated values.

The energy and density parameters most consistent with the measured monitor foil data were determined by minimizing the standard deviation of the predicted monitor reaction currents and the experimentally measured currents. Fig. 9 shows the results of this variance minimization for foil Gd-15, with the optimum incident energy being 18.05 MeV and optimum Kapton density being 96% of the nominal density. These are consistent with previous results that have shown a small reduction from the nominal Kapton density and up to a couple hundred keV variance in nominal beam energy for the 88-Inch Cyclotron (Voyles et al., 2018, 2019; Morrell et al., 2020).

Fig. 10 shows the results of the variance minimization on the current measured by the monitor reactions throughout the foil stack. After variance minimization, there is an overall reduction in the current variance throughout the stack, as seen when comparing Fig. 10 with Fig. 8. Additionally, while Fig. 8 showed an increase in current towards the rear of the stack, Fig. 10 shows a monotonic decrease in current as expected.

The proton current at each gadolinium foil location was determined using a correlated uncertainty-weighted mean of the monitor foil currents surrounding each gadolinium foil, termed a compartment for brevity, throughout the target stack (Kauermann and Carroll, 2001). The correlated uncertainty-weighted mean was calculated as:

$$\langle I \rangle = \frac{\sum_{i,j} I_j \left(\mathbf{V}_{ij}^{-1}\right)}{\sum_{i,j} \left(\mathbf{V}_{ij}^{-1}\right)}. \tag{6}$$

Accordingly, the propagated uncertainty was according to:

$$\delta I = \sqrt{\frac{1}{\sum_{i,j} \left(\mathbf{V}_{ij}^{-1}\right)}}, \tag{7}$$

where the each element ij of the covariance matrix is defined as

$$\mathbf{V}_{ij} = \sum^{\beta} \frac{dI}{d\beta_i} \sigma_{\beta_i} \Sigma_{\beta_{ij}} \sigma_{\beta_j} \frac{dI}{d\beta_j}, \tag{8}$$

where i and $j = 1, \ldots, n$, n is the number of monitor reactions in a given compartment, and $\beta \in [A_0, \rho\Delta r, \lambda, \Delta t, \int \sigma(E)\frac{d\phi}{dE} dE]$. $\Sigma_{\beta_{ij}}$ is the correlation matrix for each β. A_0 is assumed to be 30% correlated for all reactions, $\rho\Delta r$ is assumed to be 100% correlated for reactions from the same monitor foil, λ is assumed to be uncorrelated, Δt is assumed to be 100% correlated, and $\int \sigma(E)\frac{d\phi}{dE} dE$ is assumed to be 30% correlated for reactions from the same monitor foil. A linear fit was performed to the covariance-weighted compartment fluence, and the results are shown in Fig. 10. This resulted in a 641.4 ± 15.0 nAh incident fluence on the front compartment.

The data in Fig. 10 show a 2.8% drop in fluence from the Gd-01 to Gd-15. This decreasing fluence is accounted for in the measured cross-section values at each position in the foil stack, and would be erroneously neglected had an external current monitor been used to measure beam current. Fig. 10 also shows the MCNP-modeled results in comparison with the experimental results. MCNP predicts a 1% reduction in fluence throughout the stack, less than the measured 2.8%, providing additional evidence for the need of improvements in MCNP's proton transport models.

The drop in observed fluence throughout the stacked-target is due to a combination of nuclear reactions and angular scattering. The observed radiograph using the stainless steel foil at the end of the target stack indicated that angular scattering contributed a very minor amount, if any, to the overall fluence loss. However, for the MCNP model, the nuclear reaction data is generally incomplete, hence the reason for this research. This results in the use of model physics and TENDL for reaction rates and charged-particle transport in key isotopes, which has been shown to under-predict reaction rates in previous work (Hall et al., 2020). Therefore, it is not surprising that the MCNP model would under-predict the fluence drop throughout the stack, hence why it is not used for determining the fluence in this work.

2.7. Calculation of cross sections

The cross section can be calculated from the EOB activity, Eq. (2), as

$$\sigma = \frac{A_0}{I \frac{\rho\Delta r N_a}{AW}(1 - e^{-\lambda t_i}) f_{iso}}, \tag{9}$$

where A_0 is the EOB activity [Bq], I is the beam current in units of $\frac{\text{protons}}{\text{sec}}$, $\rho\Delta r$ is the areal density [g/cm^2], N_a is Avogadro's Number, AW is atomic weight, t_i is the irradiation time [s], and f_{iso} is the percent of a given isotope that occurs naturally. I was determined using the methods outlined in Sections 2.5 and 2.6; $\rho\Delta r$ for each foil is shown in Table 1. The uncertainty in the cross-section measurement is given as:

$$\delta\sigma = \sqrt{(\frac{\delta A_0}{A_0})^2 + (\frac{\delta\rho\Delta r}{\rho\Delta r})^2 + (t_i\Delta\lambda)^2 + (\frac{\delta I}{I})^2}. \tag{10}$$

Table 3
Measured cross sections of the ^{160}Gd(p, n) ^{160}Tb reaction.

Foil	Energy (MeV)	Cross section (mb)
Gd-01	17.07 ± 0.28	33.1 ± 1.0
Gd-02	16.11 ± 0.30	33.4 ± 1.0
Gd-03	15.06 ± 0.32	37.4 ± 1.1
Gd-04	14.44 ± 0.34	36.6 ± 1.2
Gd-05	13.55 ± 0.36	41.2 ± 1.2
Gd-06	12.84 ± 0.37	44.4 ± 1.3
Gd-07	12.18 ± 0.40	48.9 ± 1.4
Gd-08	11.41 ± 0.42	56.7 ± 1.8
Gd-09	10.72 ± 0.44	67.5 ± 2.0
Gd-10	9.87 ± 0.47	82.7 ± 2.4
Gd-11	9.10 ± 0.50	95.7 ± 2.8
Gd-12	8.15 ± 0.55	104.8 ± 3.0
Gd-13	7.26 ± 0.60	81.8 ± 2.8
Gd-14	6.16 ± 0.68	32.1 ± 1.0
Gd-15	5.01 ± 0.78	9.8 ± 0.3

Uncertainty in N_a, AW, and f_{iso} were neglected as insignificant. The uncertainty in $\rho\Delta r$ is determined from the propagation of uncertainty in the mass, length, and width measurements of each foil, and is shown in Table 1. Uncertainty in irradiation time δt_i is known to the second. The uncertainty in λ was taken from Reich (2005). The uncertainty in beam current δI is calculated from Eq. (7) for each gadolinium compartment, shown in Fig. 10. Finally, the uncertainty in A_0 was determined using Eq. (3).

3. Results

The experimental cross sections measured in this work are shown in Table 3. The energy uncertainty represents a one-sigma uncertainty from a Gaussian fit of the proton distribution in each foil obtained from the MCNP simulations after the variance minimization. The cross-section uncertainty is a one-sigma uncertainty resulting from the systematic and statistical error propagation in Eq. (10).

The measured cross sections are plotted in Fig. 11 in comparison with TENDL-2019 (Koning et al., 2019), Vermeulen (Vermeulen et al., 2012), and Birattari (Birattari et al., 1973). The threshold behavior below ~7 MeV closely follows the magnitude and shape measured by Birattari; TENDL evaluation appears to be half of the experimentally measured values in this region. The results from this work also indicate a larger and broader peak in the excitation function, in disagreement with TENDL predictions and the limited data from Birattari. At higher energies, above ~13 MeV, TENDL evaluations more closely match with the results of this work including similar features in increased cross section and more gradual drop which is absent in the Birattari measurements.

While the excitation function measured in this work is generally higher than the previous measurements by Birattari and Vermeulen, there are a couple of reasons for this potential disagreement. First, Birattari used a current integrator instead of monitor foils and did not account for the current drop across the aluminum degrader required to reach energies below 18 MeV at the Milan AVF cyclotron (Birattari et al., 1973). Second, an increase in the excitation function is expected based on the change in ^{160}Tb 879 keV branching ratio used in Birattari's work from 32.1% in 1973 to 30.1% in 2020 (Birattari et al., 1973; Reich, 2005).

Several nuclear data models' predicted excitation functions were compared to the results from this experiment. The default optical models and E1 gamma strength function models for each code are presented in Table 4 (Capote et al., 2009). EMPIRE, CoH, and TALYS (as well as the TALYS-generated TENDL database) are all widely-used reaction modeling codes based upon Hauser–Feshbach theory, while ALICE uses Weisskopf–Ewing calculations instead. Pre-equilibrium modeling in EMPIRE and ALICE relies upon a Hybrid Monte-Carlo Simulation model, whereas TALYS and ALICE use a two-component exciton pre-equilibrium model.

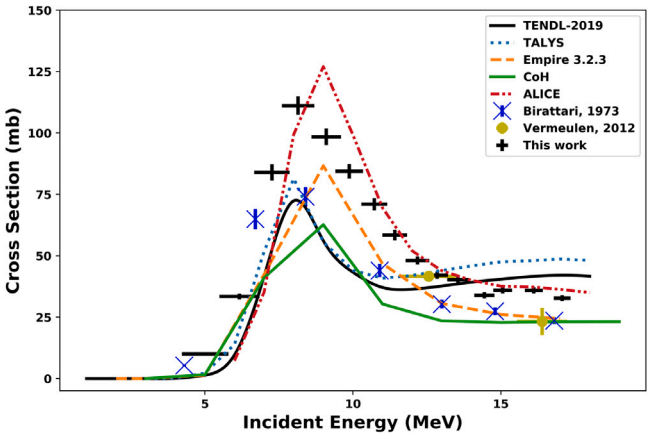

Fig. 11. ^{160}Gd(p, n) cross sections obtained from this work compared to TENDL-2019 (Koning et al., 2019), previous experimental data from Birattari and Vermeulen (Vermeulen et al., 2012; Birattari et al., 1973), and modeled results using ALICE, CoH, Empire 3.2.3, and TALYS (Blann and Bisplinghoff, 1982; Kawano et al., 2010; Herman et al., 2007; Koning and Rochman, 2012).

Fig. 11 shows a comparison between each of the data models, the previous experimental points, and the data from this experiment. In general, using default parameters, all models fail to consistently (within 20%) reproduce the experimental data, including both the results presented in this work, as well as prior measurements. For the present case, modeling is restricted to a single target isotope without any competing channels leading to the same residual product, both of which avoid additional complexity in such "cumulative" reaction modeling of multiple separate channels leading to ^{160}Tb. While low-energy (p, n) modeling presents a relatively easy challenge, the static deformation of the ^{160}Gd(p, n) target adds an additional complexity, necessitating the use of coupled-channel calculations for this multiple-exciton process, to extend the optical models used for spherical nuclei. Even in this context, all models exhibit very poor predictive power.

Of the models, TALYS/TENDL both do the best job of reproducing the compound peak observed near 8 MeV in the experimental data, but underestimate the magnitude of this peak, for both the present data, as well as that of Birattari. ALICE and EMPIRE do a better job with the magnitude of the compound peak, though their prediction of the peak at higher energies when compared to the experimental data suggests a suppression of the incoming particle channel, leading to an enhanced effective energetic threshold. CoH fails to reproduce both the location and magnitude of the compound peak, clearly performing the worst of these models presented here.

Moving to higher energies, it is apparent that ALICE does an excellent job of reproducing both the shape and magnitude of the pre-equilibrium tail for the data presented in this work, and EMPIRE does the same for the Birattari data. Despite the small number of data points in this energy region, the Vermeulen data appears to suggest a tail shape with a transition between those of ALICE and EMPIRE. The tail shape for TALYS/TENDL surprisingly predicts the growth of a secondary peak near 18 MeV, a feature not observed in any of the experimental data, suggesting that these models underestimate other channels in this energy region. As with the compound peak, CoH fails to reproduce both the shape and magnitude of the pre-equilibrium, suggesting that it overpredicts the feeding of other channels in this energy region.

Based on this comparison, it is difficult to declare any of these models as clearly superior in terms of predictive power. However, as has been seen in recent work (Voyles et al., 2018, 2019; Fox et al., 2020), the default predictive power of these codes, even for strongly-fed channels, often holds only locally and does not extend to adjacent channels. This problem exhibits a complex residual topology for any

Table 4
Default settings for the reaction codes.

Code version	Proton/Neutron optical model	Alpha Optical Model	E1 γSF model	Level density model
EMPIRE-3.2.3 (Herman et al., 2007)	Koning–Delaroche (Koning and Delaroche, 2003)	Avrigeanu (2009) (Avrigeanu et al., 2009)	Modified Lorentzian (Belgya et al., 2006)	Empire (Herman et al., 2007, 2013)
TALYS-1.9 (Koning and Rochman, 2012)	Koning–Delaroche	Specific folded potential (Koning and Rochman, 2012)	Brink-Axel Lorentzian (Koning and Rochman, 2012)	Gilbert & Cameron (Gilbert and Cameron, 1965)
CoH-3.5.3 (Kawano, 2003; Kawano et al., 2010)	Koning–Delaroche	Avrigeanu (1994) (Avrigeanu et al., 1994)	Generalized Lorentzian (Kawano, 2003; Kawano et al., 2010)	Gilbert & Cameron
ALICE-2017 (Blann, 1996)	Nadasen (Nadasen et al., 1981)	Parabolic Diffuse-Well (Darrah Thomas, 1959)	Berman–Fultz Lorentzian (Berman and Fultz, 1975)	KRK (Kataria et al., 1978)

global optimization, as these channels are both highly correlated and constrained, leading to high sensitivity in seeking a global minimum in parameter space. As this is not a trivial process, this provides further evidence that further channel observations (including all dominant channels), are needed to improve the default predictive power for reaction modeling of rare-earth nuclei in these models.

4. Conclusion

This work reports the ^{160}Gd(p, n) ^{160}Tb excitation function between 4–18 MeV obtained using stacked-target activation at Lawrence Berkeley National Laboratory's 88-Inch Cyclotron. In post-detonation nuclear forensics, the ratio of ^{161}Tb: ^{160}Tb allows for background correction of ^{161}Tb, an important fission product for fission split determination. The cross sections results reported in this work represent improvements in number, precision, and uncertainty quantification over previous experimental measurements thereby enabling optimizing of the production of post-detonation surrogate debris samples and improved analysis of detonation debris for nuclear forensics and attribution.

A priori predictions of the ^{160}Gd(p, n) reaction using default parameters for ALICE, CoH, EMPIRE, and TALYS, as well as the TENDL database, are compared to the experimentally measured values. In all cases, the four codes had difficulty reproducing the magnitude and shape of the excitation function reported across the energy range considered in this work. For the compound peak observed near 8 MeV, ALICE and EMPIRE do a reasonable job with the magnitude of the compound peak, but both appear to suggest a suppression of the incoming particle channel, resulting in a shift of the peak and a higher effective energetic threshold. At higher energies (> 10 MeV), ALICE does an excellent job of reproducing both the shape and magnitude of the pre-equilibrium tail. This highlights the issue that, even for strongly-fed channels, the default predictive power of these codes, is often localized and not generalizable for rare-earth nuclei.

This work focused on presenting the ^{160}Gd(p, n) reaction important for post-detonation forensics, but additional data was obtained for ^{nat}Gd(p, x) channels in this energy range. Future work will interpret and present the results from all (p, x) reaction channels measured. Several of these channels have limited to no measured data available, thereby providing data to further constrain nuclear data evaluations and codes in this energy range for rare-earth nuclei.

CRediT authorship contribution statement

Ryan K. Chapman: Methodology, Software, Formal analysis, Investigation, Writing - original draft, Visualization. **Andrew S. Voyles:** Methodology, Software, Investigation, Writing - review & editing. **Narek Gharibyan:** Conceptualization, Software, Writing - review & editing. **Lee A. Bernstein:** Conceptualization, Resources. **James E. Bevins:** Conceptualization, Methodology, Validation, Resources, Writing - review & editing, Supervision, Project administration, Funding acquisition.

Declaration of competing interest

The authors declare that they have no known competing financial interests or personal relationships that could have appeared to influence the work reported in this paper.

Acknowledgments

The authors would like to thank the 88-Inch Cyclotron staff for their help and support in performing this research. Additional assistance on this research was provided by Dr. Abigail Bickley (AFIT) and Dr. John McClory (AFIT).

This work is supported by the U.S. Air Force Technical Application Center (AFTAC) under the AFIT/AFTAC Endowed Term Chair MOA#: 212196. This work was performed under the auspices of the U.S. Department of Energy by Lawrence Livermore National Laboratory under Contract DE-AC52-07NA27344 and Lawrence Berkeley National Laboratory, USA under Contract DE-AC02-05CH11231. This work was also partially supported by the U.S. Department of Energy Isotope Program, managed by the Office of Science. The views expressed in this article are those of the authors and do not necessarily reflect the official policy or position of the United States Air Force, the Department of Defense, or the United States Government.

References

Anon, 2010. Nuclear Forensics: A Capability At Risk. The National Academies Press, Washington, DC.

Anon, 2015. In: Fedchenko, V. (Ed.), The New Nuclear Forensics: Analysis of Nuclear Materials for Security Purposes. Oxford University Press, Solna, Sweden.

Anon., 2017. In: Werner, C.J. (Ed.), MCNP Users Manual - Code Version 6.2. LA-UR-17-29981.

Avrigeanu, V., Hodgson, P.E., Avrigeanu, M., 1994. Global optical potentials for emitted alpha particles. Phys. Rev. C 49 (4), 2136–2141. http://dx.doi.org/10.1103/PhysRevC.49.2136.

Avrigeanu, M., Obreja, A.C., Roman, F.L., Avrigeanu, V., von Oertzen, W., 2009. Complementary optical-potential analysis of α-particle elastic scattering and induced reactions at low energies. At. Data Nucl. Data Tables 95 (4), 501–532. http://dx.doi.org/10.1016/j.adt.2009.02.001.

Belgya, T., Bersillon, O., Capote, R., 2006. Handbook for Calculations of Nuclear Reaction Data, RIPL-2. IAEA-TECDOC-1506. IAEA, Vienna.

Berman, B.L., Fultz, S.C., 1975. Measurements of the giant dipole resonance with monoenergetic photons. Rev. Modern Phys. 47 (3), 713–761. http://dx.doi.org/10.1103/RevModPhys.47.713.

Birattari, C., Gadioli, E., Gadioli Erba, E., Grassi Strini, A.M., Strini, G., Tagliaferri, G., 1973. Pre-equilibrium processes in (p, n) reactions. Nucl. Phys. A 201, 579–592.

Blann, M., 1996. New precompound decay model. Phys. Rev. C 54 (3), 1341–1349. http://dx.doi.org/10.1103/PhysRevC.54.1341.

Blann, M., Bisplinghoff, J., 1982. Code: ALICE/LIVERMORE 82. Lawrence Livermore National Laboratory. unpublished.

Brown, F.B., Sweezy, J.E., Hayes, R., 2004. Monte Carlo parameter studies and uncertainty analyses with MCNP5, in: Proceedings of the PHYSOR 2004: The Physics of Fuel Cycles and Advanced Nuclear Systems - Global Developments, pp. 121–129.

Brown, E.J., Tuli, J.K., 2010. Nuclear data sheets for A=65. Nucl. Data Sheets 111 (9), 2425–2553. http://dx.doi.org/10.1016/j.nds.2010.09.002.

Burrows, T.W., 2006. Nuclear data sheets for A=48. Nucl. Data Sheets 107 (7), 1747–1922. http://dx.doi.org/10.1016/j.nds.2006.05.005.

Capote, R., Herman, M., et al., 2009. RIPL — Reference input parameter library for calculation of nuclear reactions and nuclear data evaluations. Nucl. Data Sheets 110 (12), 3107–3214. http://dx.doi.org/10.1016/j.nds.2009.10.004.

Covo, M.K., Albright, R.A., et al., 2018. 88-inch cyclotron: The one-stop facility for electronics radiation testing. Measurement 127, 580–587.

Darrah Thomas, T., 1959. Cross section for compound-nucleus formation in heavy-ion-induced reactions. Phys. Rev. 116 (3), 703–712. http://dx.doi.org/10.1103/PhysRev.116.703.

Fox, Morgan B., Voyles, Andrew S., Morrell, Jonathan T., Bernstein, Lee A., Am-Lewis, anda M., Koning, Arjan J., Batchelder, Jon C., Birnbaum, Eva R., Cutler, Cathy S., Medvedev, Dmitri G., Nortier, Francois M., Ellen M. O'Brien, Vermeulen, Christiaan, 2020. Christiaan vermeulen investigating high-energy proton-induced reactions on spherical nuclei: Implications for the pre-equilibrium exciton model. arXiv:2010.12790v1.

Gilbert, A., Cameron, A.G.W., 1965. A composite nuclear-level density formula with shell corrections. Can. J. Phys. 43 (8), 1446–1496. http://dx.doi.org/10.1139/p65-139.

Graves, S.A., Ellison, P.A., et al., 2016. Nuclear excitation functions of proton-induced reactions (E_p=35–90 MeV) from Fe, Cu, and Al. Nucl. Instrum. Methods Phys. Res. B 386, 44–53. http://dx.doi.org/10.1016/j.nimb.2016.09.018.

Hall, Amy, Gum, Daniel A., Ferrieri, Richard A., Brockman, John, Bevins, James E., 2020. Development of an experimentally-validated MCNP6 model for ^{1}1C production via the ^{1}4N(p, α) reaction using a GE PETTrace cyclotron. Nucl. Technol. http://dx.doi.org/10.1080/00295450.2020.1740561.

Herman, M., Capote, R., Carlson, B.V., Oblozinsky, P., Sin, M., Trkov, A., Wienke, H., Zerkin, V., 2007. EMPIRE: Nuclear reaction model code system for data evaluation. Nucl. Data Sheets 108 (12), 2655–2715. http://dx.doi.org/10.1016/j.nds.2007.11.003.

Herman, M., et al., 2013. EMPIRE-3.2 Malta: Modular System for Nuclear Reaction Calculations and Nuclear Data Evaluation.

Hermanne, A., et al., 2018. Reference cross sections for charged-particle monitor reactions. Nucl. Data Sheets 148, 338–382.

Joint Nuclear Forensics Working Group of the American Physical Society and the American Association for the Advancement of Science, 2013. Nuclear Forensics: Role, State of the Art, and Program Needs.

Kataria, S.K., Ramamurthy, V.S., Kapoor, S.S., 1978. Semiempirical nuclear level density formula with shell effects. Phys. Rev. C 18 (1), 549–563. http://dx.doi.org/10.1103/PhysRevC.18.549.

Kauermann, G., Carroll, R.J., 2001. A note on the efficiency of sandwich covariance matrix estimation. J. Amer. Statist. Assoc. 96 (456), 1387–1396. http://dx.doi.org/10.2307/3085907.

Kawano, Toshihiko, 2003. CoH: The Hauser–Feshbach-Moldauer statistical model with the coupled-channels theory, Los Alamos National Laboratory, unpublished.

Kawano, T., Talou, P., Chadwick, M.B., Watanabe, T., 2010. Monte Carlo simulation for particle and γ-ray emissions in statistical Hauser–Feshbach Model. J. Nucl. Sci. Technol. 47 (5), 462–469. http://dx.doi.org/10.1080/18811248.2010.9711637.

Kis, Z., Fazekas, N., Östör, J., Révay, Z., Belgya, T., Molnár, G.L., Koltay, L., 1998. Comparison of efficiency functions for Ge gamma-ray detectors in a wide energy range. Nucl. Instrum. Methods Phys. Res. A 418 (2–3), 374–386. http://dx.doi.org/10.1016/S0168-9002(98)00778-5.

Koning, A.J., Delaroche, J.P., 2003. Local and global nucleon optical models from 1 keV to 200 MeV. Nucl. Phys. A 713 (3–4), 231–310. http://dx.doi.org/10.1016/S0375-9474(02)01321-0.

Koning, A.J., Rochman, D., 2012. Modern nuclear data evaluation with the TALYS code system. Nucl. Data Sheets 113 (12), 2841–2934. http://dx.doi.org/10.1016/j.nds.2012.11.002.

Koning, A.J., Rochman, D., Sublet, J., Dzysiuk, N., Fleming, M., van der Marck, S., 2019. TENDL: Complete nuclear data library for innovative nuclear science and technology. Nucl. Data Sheets 155.

Morrell, J.T., Voyles, A.S., et al., 2020. Measurement of ^{139}La(p, x) cross sections from 35–60 MeV by stacked-target activation. Eur. Phys. J. A 56 (13), http://dx.doi.org/10.1140/epja/s10050-019-00010-0.

Nadasen, A., Schwandt, P., Singh, P.P., Jacobs, W.W., Bacher, A.D., Debevec, P.T., Kaitchuck, M.D., Meek, J.T., 1981. Elastic scattering of 80–180 MeV protons and the proton–nucleus optical potential. Phys. Rev. C 23 (3), 1023–1043. http://dx.doi.org/10.1103/PhysRevC.23.1023.

Nethaway, D.R., 1985. Fission split and the ^{161}Tb soil correction. FP-44-85-139.

Reich, C.W., 2005. Nuclear data sheets for A=160. Nucl. Data Sheets 105 (3), 557–774. http://dx.doi.org/10.1016/j.nds.2005.08.001.

Rooney, B., Felsher, P., 2018. Peakeasy. [Online], Available: https://peakeasy.lanl.gov/.

Vermeulen, C., Steyn, G.F., et al., 2012. Cross sections of proton-induced reactions on ^{nat}Gd with special emphasis on the production possibilities of ^{152}Tb and ^{155}Tb. Nucl. Instrum. Methods Phys. Res. B 275, 24–32. http://dx.doi.org/10.1016/j.nimb.2011.12.064.

Voyles, L.A., Bernstein, A.S., et al., 2018. Excitation functions for (p, x) reactions of niobium in the energy range of E_p = 40–90 MeV. Nucl. Instrum. Methods Phys. Res. B 429, 53–74.

Voyles, A.S., Lewis, A.M., et al., 2019. Proton-induced reactions on Fe, Cu, & Ti from threshold to 55 MeV. ArXiv. Available: http://arxiv.org/abs/1910.11135.

Wu, S.C., 2000. Nuclear data sheets for A=46. Nucl. Data Sheets 91 (1), 1–116. http://dx.doi.org/10.1006/ndsh.2000.0014.